Earth and Planetary Science Letters 453 (2016) 33–43

Contents lists available at ScienceDirect

Earth and Planetary Science Letters

www.elsevier.com/locate/epsl

Regolith evolution on the millennial timescale from combined U–Th–Ra isotopes and in situ cosmogenic ^{10}Be analysis in a weathering profile (Strengbach catchment, France)

J. Ackerer [a,*], F. Chabaux [a,*], J. Van der Woerd [b], D. Viville [a], E. Pelt [a], E. Kali [b], C. Lerouge [c], P. Ackerer [a], R. di Chiara Roupert [a], P. Négrel [c]

[a] Laboratoire d'Hydrologie et de Géochimie de Strasbourg (LHyGeS), CNRS UMR 7517, University of Strasbourg, 1 rue Blessig, 67084 Strasbourg cedex, France
[b] Institut de Physique du Globe de Strasbourg (IPGS), CNRS UMR 7516, University of Strasbourg, 5 rue René Descartes, 67084 Strasbourg cedex, France
[c] BRGM, 3 Avenue Claude Guillemin, 45060 Orléans, France

ARTICLE INFO

Article history:
Received 25 February 2016
Received in revised form 2 August 2016
Accepted 4 August 2016
Available online xxxx
Editor: D. Vance

Keywords:
regolith
weathering
denudation
U-series nuclides
in situ ^{10}Be

ABSTRACT

U–Th–Ra disequilibria, cosmogenic in situ ^{10}Be concentrations and major and trace element concentrations have been analyzed in a 2 m-deep weathering profile sampled at the summit of the granitic Strengbach catchment (France). The data have been used to independently estimate both the long-term regolith production and denudation rates and the weathering and erosion rates. Modeling of the ^{238}U–^{234}U–^{230}Th–^{226}Ra disequilibrium variations in the lower part of the profile yields a regolith production rate of 12 ± 4 mm/kyr (30 ± 10 T/km^2/yr), while modeling of the high-resolution ^{10}Be concentration profile leads to an exposure age of 19.7 ± 2.2 kyr, an inherited concentration of 15,000 ± 1,000 at/g in quartz and a mean denudation rate of 22 ± 10 mm/kyr (37 ± 15 T/km^2/yr). The consistency between production and denudation rates suggests that, on a millennial timescale, the regolith mass balance at the summit of the catchment is close to a steady state, even if the watershed may have been impacted by Quaternary climatic changes and by recent anthropogenic perturbations (e.g., 20th century acid rain and recent afforestation efforts). The results also indicate that physical erosion is likely the dominant long-term process of regolith denudation in the catchment. Furthermore, the comparison of the long-term production and denudation rates and of weathering and erosion rates determined from the depth profile analyses with the current weathering and erosion rates estimated at the outlet of the watershed based on monitoring of the water chemistry and sediment fluxes suggests that physical erosion may have varied more than the chemical weathering flux during the last 150 kyr. Although very few other sites with U-series, in situ ^{10}Be and stream monitoring data are available for comparison, the current data suggest that (1) the mass balance steady state of regolith might be commonly achieved in soil mantled landscapes, and (2) physical erosion has varied much more than chemical weathering in mid-mountain catchments over the last 10–150 kyr. These results highlight the importance of the combined analysis of U-series nuclides and in situ ^{10}Be in the same weathering profile for the determination of key geomorphic parameters, which are important to constraining landscape stability and the responses of landscapes to natural or anthropogenic forcing.

1. Introduction

Regolith production and denudation rates, which correspond to the rate at which bedrock is weathered into mobile regolith and removed by chemical and physical processes, are key parameters in the evaluation of landscape stability and the responses of landscapes to natural or anthropogenic forcing (e.g., Brantley et al., 2007; Banwart et al., 2011). The analytical developments made over the last decades for precisely analyzing the U-series nuclides (i.e., ^{238}U–^{234}U–^{230}Th) in geological and environmental samples have led to the development of the study of U-series nuclides in soils and weathering profiles and to the definition of a theoretical framework for quantifying regolith production rates from the variations in radioactive disequilibria along a weathering profile (Dequincey et al., 2002; Chabaux et al., 2003, 2013; Dosseto et al., 2008, 2012; Ma et al., 2010). These studies were mainly

* Corresponding authors.
E-mail addresses: julien.ackerer2@etu.unistra.fr (J. Ackerer), fchabaux@unistra.fr (F. Chabaux).

http://dx.doi.org/10.1016/j.epsl.2016.08.005
0012-821X/

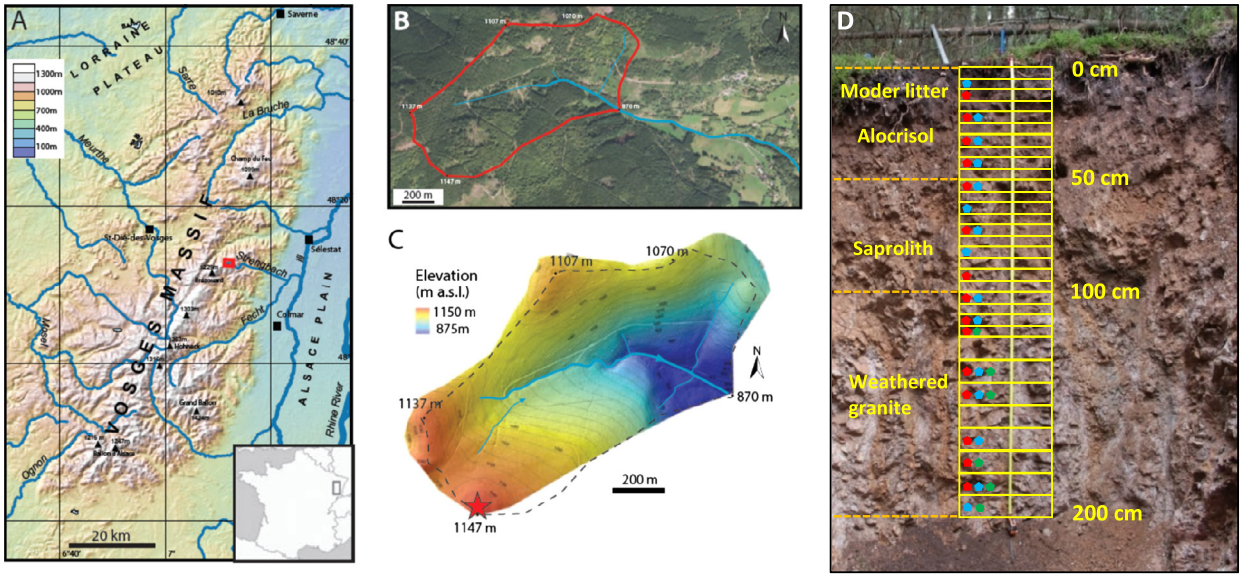

Fig. 1. a) Regional map of the Vosges massif and location of the Strengbach catchment. b) Contour of the Strengbach watershed. c) Topographic map of the Strengbach watershed and location of the studied weathering profile (map from OHGE). d) Sampling of the weathering profile. The pedological observation led to division of the weathering profile into 3 zones: the soil from 0 to 50 cm, the saprolite from 50 to 100 cm and the granitic weathered bedrock from 100 to 200 cm. Each box in the column represents a collected sample. Red and blue dots indicate samples for which isotopic U–Th–Ra and in situ ^{10}Be analyses have been performed, respectively. Green dots indicate samples for which thin sections have been performed. (For interpretation of the references to color in this figure legend, the reader is referred to the web version of this article.)

based on the analysis of ^{238}U–^{234}U–^{230}Th nuclides and the use of the activity ratios (^{234}U/^{238}U)–(^{230}Th/^{234}U) (activity ratios will be noted hereafter with parentheses). More recently, some studies have also included the analysis of the ^{226}Ra nuclide and hence the use of the (^{226}Ra/^{230}Th) ratio (Chabaux et al., 2013; Gontier et al., 2015). Similarly, the in situ ^{10}Be depth profile methodology has enabled the estimation of both exposure age and mean denudation rate from cosmogenic isotope inventories (e.g., Brown et al., 1995; Braucher et al., 2009). This approach has been widely used to constrain the ages of alluvial terraces and fans (Anderson et al., 1996; Schaller et al., 2002; Brocard et al., 2003), as well as the long-term denudation rates of regolith (Small et al., 1999; Heimsath et al., 2000; Ferrier and Kirchner, 2008; Cui et al., 2016). However, very few studies have combined a detailed analysis of U–Th–Ra isotopes with cosmogenic in situ ^{10}Be in a single weathering profile extending from the topsoil to the bedrock. It is the aim of this work to highlight the potential of combining these two approaches to independently constrain both production and denudation rates of regolith and to show that information associated with geochemical mobility can be used to discuss the long-term evolution of the regolith.

2. Site presentation and sampling strategy

The study is performed on the Strengbach catchment, which constitutes the "Observatoire Hydrogéochimique de l'Environnement" (OHGE), one of the French critical zone observatories (http://rnbv.ipgp.fr). It is a small watershed of 0.8 km^2 located in the Vosges massif (northeastern France; Fig. 1A). With altitudes ranging from 883 to 1147 m (Figs. 1B and 1C), the current climate is mountainous-oceanic, with a mean annual rainfall and temperature of 1400 mm and 6 °C, respectively (Viville et al., 2012). The Vosges massif experienced Pleistocene glaciations in a similar way to other central European mountains, such as the Black Forest and the Bavarian Forest (Heyman et al., 2013). In accordance with regional climatic studies (e.g., Leroy et al., 2000), cold conditions probably persisted at the altitude of the Strengbach catchment well after the Late Glacial Maximum (LGM), and the Vosges forest cover likely developed only at the onset of the Holocene. The Strengbach site has been affected by anthropogenic deforestation associated with pastoralism, likely beginning in the Bronze Age and lasting until the end of the 19th century (Etienne et al., 2013). In the 20th century, the lower grazing pressure led to natural and artificial afforestation in several places in the Vosges massif. In the Strengbach catchment, the return to a densely forested cover is due to the planting of spruce stands at the beginning of the 20th century. The catchment is currently covered with a mixed spruce and beech forest interspersed with small clearings. The bedrock is a base-poor late Hercynian granite and is covered by a 50 to 100 cm-thick brown acidic soil (Hyperdystric Cambisol; WRB, 2006). The granitic bedrock was hydrothermally overprinted, with the degree of hydrothermal alteration decreasing from the northern to the southern part of the watershed (Fichter et al., 1998).

To investigate the recent Quaternary weathering of the granitic bedrock and the denudation rate of the soil, a sampling profile has been collected on the summit of the less hydrothermally altered part of the watershed. This location avoids the presence of colluvial deposition and corresponds to the best strategy ensuring that saprolite and soil are genetically linked to the underlying bedrock and likely formed along the main vertical weathering direction. A 2 m-deep and 3 m-wide pit was dug, and the samples were collected in the middle part of the pit front (Fig. 1D). Thirty-two bulk samples of ≈5 kg each were collected along the profile with a sample every 5 cm within the soil and the saprolite and every 10 cm within the fractured bedrock. The large mass collected per sample is necessary to ensure a representative analysis of the weathering profile developed on the coarse-grained granite (Gy, 1992). For each sample in the upper part of the profile (0–100 cm), the fine fraction density was obtained by weighing a known volume of soil sampled with a steel cylinder. The proportion of blocks, defined here as coarse fragments (>10 cm), was estimated via macroscopic description and photos. The bulk density of each sample was then calculated by combining the fine fraction density and the density of blocks with respect to the proportion of blocks in the horizon. For the blocks, a constant density of 2700 kg/m^3 is used, on the basis of granitic bedrock density measurements. A sequential crushing and rigorous quartering process was then performed to obtain representative subsamples for min-

Table 1
Some chemical and physical characteristics of the studied weathering profile. Major and trace element concentrations were determined by conventional tetraborate alkaline fusion followed by mass spectrometry and atomic emission spectrometry measurements (ICP-MS and ICP-AES procedure) (uncertainty <5% for major element and <10% for trace element concentrations). STR13-53[2] is a dissolution powder duplicate. STR13-53[3] is a quartering duplicate that encompasses the whole crushing process.

Sample	Depth (cm)	Type	Bulk density (g/cm^3)	SiO_2 (%)	Al_2O_3 (%)	CaO (%)	Na_2O (%)	K_2O (%)	MgO (%)	Fe_2O_3 (%)	MnO (%)	TiO_2 (%)	P_2O_5 (%)	LOI (1000 °C) (%)	Ta (mg/kg)	Zr (mg/kg)
STR13-41	12.5	Soil	1.0	73.20	12.05	0.16	1.70	4.55	0.21	1.30	0.011	0.18	0.27	4.79	2.3	81.0
STR13-43	22.5	Soil	1.5	69.30	13.49	0.18	2.10	4.96	0.26	1.71	0.021	0.21	0.48	5.51	2.7	73.0
STR13-45	32.5	Soil	1.2	68.50	14.03	0.27	2.40	4.99	0.32	1.69	0.027	0.22	0.59	4.85	2.9	70.0
STR13-47	42.5	Soil	1.7	68.10	14.72	0.33	2.66	5.19	0.36	1.70	0.034	0.22	0.56	4.08	2.4	71.0
STR13-49	52.5	Soil	1.7	70.20	13.99	0.29	2.45	5.09	0.30	1.53	0.032	0.20	0.50	3.22	2.7	67.0
STR13-51	62.5	Saprolite	2.0	70.10	14.36	0.34	2.57	5.05	0.34	1.57	0.032	0.20	0.51	2.96	2.7	62.0
STR13-53	72.5	Saprolite	2.1	70.60	14.08	0.23	2.25	5.30	0.26	1.59	0.030	0.18	0.41	2.52	2.7	62.0
STR13-53[2]	72.5	Saprolite	2.1	71.20	13.94	0.32	2.39	5.07	0.34	1.60	0.030	0.19	0.42	–	–	–
STR13-53[3]	72.5	Saprolite	2.1	70.70	13.77	0.34	2.47	5.09	0.34	1.58	0.030	0.18	0.42	–	–	–
STR13-55	82.5	Saprolite	2.1	69.50	14.76	0.29	2.30	5.13	0.39	2.04	0.037	0.22	0.42	2.82	3.3	67.0
STR13-57	92.5	Saprolite	2.4	69.60	14.56	0.32	2.45	5.18	0.39	2.08	0.028	0.20	0.35	2.39	3.1	61.0
STR13-59	102.5	Bedrock	2.5	70.20	14.87	0.35	2.58	5.23	0.20	1.82	0.023	0.20	0.35	2.26	3.1	64.0
STR13-61	112.5	Bedrock	2.6	71.80	14.50	0.30	2.20	5.34	0.20	1.38	0.020	0.16	0.39	2.17	2.8	67.0
STR13-41B	117.5	Bedrock	2.7	71.60	14.80	0.30	2.50	5.35	0.20	1.19	0.020	0.15	0.34	1.97	2.5	64.0
STR13-42B	135	Bedrock	2.7	72.60	14.30	0.30	2.30	5.23	0.25	1.31	0.022	0.18	0.31	1.87	2.6	67.0
STR13-43B	145	Bedrock	2.7	72.60	14.38	0.28	2.37	5.10	0.26	1.25	0.027	0.17	0.33	1.59	2.8	70.0
STR13-45B	165	Bedrock	2.7	72.10	14.19	0.26	2.22	5.16	0.20	1.41	0.032	0.16	0.31	1.83	2.6	77.0
STR13-46B	175	Bedrock	2.7	71.80	14.20	0.30	2.60	5.46	0.26	1.27	0.017	0.15	0.33	1.7	2.5	70.0
STR13-47B	185	Bedrock	2.7	72.40	14.38	0.28	2.33	5.13	0.39	1.16	0.016	0.16	0.32	1.57	2.7	69.0

eralogical analyses by X-ray diffraction (XRD), and for geochemical and isotopic analyses.

3. Analytical methods

3.1. Mineralogical and major and trace element analysis

The sample mineralogical determination and compositions are given in the Electronic Supplement. Six thin sections of rock samples were collected at regular intervals within the granitic bedrock (Fig. 1D). Major and trace element concentrations of the samples were analyzed following the technique classically used at the LHyGeS (Strasbourg, France; e.g., Prunier et al., 2015). The quality of the analysis was checked by measuring the San Joaquin soil standard (NIST SRM 2709a). The overall uncertainty is <5% for the major element and <10% for the trace element concentrations (Table 1).

3.2. U–Th–Ra isotopes

For the U–Th–Ra analysis, each subsample consists of approximately 100 mg of 53 µm powdered bulk sample. Subsamples were weighed and spiked with both a mixed artificial ^{233}U–^{229}Th spike and a ^{228}Ra enriched spike to measure the isotopic ratios and U–Th–Ra concentrations by isotopic dilution, using the protocol developed in the LHyGeS (Strasbourg, France; Granet et al., 2010; Chabaux et al., 2013; Pelt et al., 2013). The powders were first digested in PFA beakers using combinations of HF, HNO_3, HCl, $HClO_4$ and H_3BO_3 acids at 100–200 °C, and U, Th, and Ra were then separated and purified by ion exchange chromatography using Biorad anionic resin. U and Th isotopes were measured on a plasma mass spectrometer (MC-ICP-MS Neptune), and the ^{226}Ra isotope was measured on a thermal ionization mass spectrometer (TIMS Triton, Table 2). The precision and accuracy of the analyses are checked by regular analysis of liquid standards (HU1 U, IRMM036 Th and ^{228}Ra-spike), the rock standard BCR-2 and sample replicates. The ($^{234}U/^{238}U$) activity ratio was 0.9992 ± 0.0018 for HU1 (2σ, $N = 19$) and the $^{232}Th/^{230}Th$ isotope ratio was 326284 ± 2855 for IRMM036 (2σ, $N = 21$). The ($^{234}U/^{238}U$), ($^{230}Th/^{234}U$), ($^{230}Th/^{232}Th$) and ($^{226}Ra/^{230}Th$) activity ratios for BCR-2 were 1.0028 ± 0.0018, 1.0045 ± 0.0104, 0.8824 ± 0.0076 and 0.9946 ± 0.0078 (2σ, $N = 2$), respectively. The mean U and Th blank concentrations were 46 pg and 157 pg, respectively, whereas the Ra concentrations were below the detection limit. These blank concentrations were all negligible compared to the measured quantities of U, Th and Ra. Inter-session standard and duplicate measurements enabled estimation of the analytical uncertainty in the calculated U–Th–Ra radioactive activity ratios. The analytical uncertainty is 0.2% for ($^{234}U/^{238}U$), 1.5% for ($^{230}Th/^{234}U$) and 1.7% for ($^{226}Ra/^{230}Th$) activity ratios.

3.3. In situ ^{10}Be isotope

For the in situ ^{10}Be analysis, each subsample consists of 150 g of 250–500 µm sieved powder obtained from quartering the 2 mm crushed bulk samples. Oxides and organic matter were removed by HCl leaching, and a sequential HF dissolution was performed to remove the meteoric ^{10}Be and obtain purified quartz (e.g., Nishiizumi et al., 1989). After addition of a ^{9}Be carrier, the purified quartz was dissolved, and beryllium separation and purification were performed by ion exchange chromatography. After hydroxylation and targeting, the $^{10}Be/^{9}Be$ ratios were measured by accelerator mass spectrometry at ASTER (CEREGE, University of Aix-Marseille, France). The $^{10}Be/^{9}Be$ ratios of the blanks and samples are approximately 1×10^{-15} and 1×10^{-13}, respectively. The overall analytical uncertainty is <5% for the calculated ^{10}Be concentrations (Table 3).

4. Determination of the regolith production rate, denudation rate and chemical mobility

4.1. Regolith production rate from U–Th–Ra disequilibria

The principle of determination of the regolith production rate from the analysis of U–Th–Ra disequilibria has been detailed in previous studies (e.g., Dosseto et al., 2008, 2012; Ma et al., 2010; Chabaux et al., 2011, 2013). The approach is based on the analysis of samples collected along the main weathering direction, in the present case the vertical direction. For samples in the weathering zone, as the time variation of nuclide mobility during water rock interactions is not known *a priori*, the time evolution of radioactive nuclides is classically described in terms of continuous processes involving, in addition to the radioactive decay laws, loss and gain processes represented by first-order kinetic rate laws for the loss processes and zero-order kinetic rate laws for the gain processes.

Table 2
U-series data. U and Th concentrations are calculated from isotopic dilution. The uncertainties are at the 2σ level: 0.2% and 0.5% for U and Th concentrations, 0.2% for (^{234}U/^{238}U), 1% for (^{230}Th/^{232}Th), 1.5% for (^{230}Th/^{234}U) and 1.7% for (^{226}Ra/^{230}Th) activity ratios. STR13-53[2] is a dissolution powder duplicate. STR13-53[3] is a quartering duplicate that encompasses the whole crushing process. For the activity ratio calculation, the following radioactivity constants were used: $\lambda_{232} = 4.948 \times 10^{-11}$ yr^{-1}, $\lambda_{230} = 9.158 \times 10^{-6}$ yr^{-1}, $\lambda_{234} = 2.826 \times 10^{-6}$ yr^{-1}, $\lambda_{238} = 1.551 \times 10^{-10}$ yr^{-1}, and $\lambda_{226} = 4.335 \times 10^{-4}$ yr^{-1} (Akovali, 1996; Cheng et al., 2000).

Sample	Depth (cm)	U (mg/kg)	Th (mg/kg)	(^{234}U/^{238}U)	(^{230}Th/^{232}Th)	(^{230}Th/^{234}U)	(^{226}Ra/^{230}Th)
STR13-41	12.5	3.417	7.800	1.021	1.412	1.036	0.986
STR13-43	22.5	3.621	8.904	1.026	1.433	1.130	1.027
STR13-45	32.5	4.224	9.752	1.025	1.495	1.105	0.928
STR13-47	42.5	3.830	9.636	1.029	1.440	1.158	0.974
STR13-49	52.5	3.763	9.179	1.024	1.471	1.150	0.992
STR13-53	72.5	3.528	8.622	1.034	1.486	1.156	0.931
STR13-53[2]	72.5	3.575	8.643	1.032	1.499	1.155	0.936
STR13-53[3]	72.5	3.462	8.699	1.034	1.454	1.162	0.936
STR13-57	92.5	3.841	9.387	1.040	1.519	1.175	0.944
STR13-59	102.5	4.155	9.810	1.036	1.544	1.158	0.949
STR13-61	112.5	3.884	9.111	1.025	1.517	1.140	0.966
STR13-41B	117.5	3.531	8.753	1.016	1.392	1.114	0.999
STR13-42B	135	3.957	8.433	1.024	1.623	1.109	0.963
STR13-43B	145	4.294	9.659	1.015	1.504	1.094	0.963
STR13-45B	165	4.601	9.193	1.011	1.653	1.072	0.984
STR13-46B	175	4.470	9.415	1.006	1.531	1.052	1.008
STR13-47B	185	4.269	9.149	0.987	1.451	1.034	0.988

Table 3
In situ ^{10}Be data for the studied weathering profile. The elevation is 1147 m a.s.l. The latitude and longitude are 48°12′29.4″N and 7°11′30.3″E, respectively. There is no shielding correction due to the summit location of the profile. The surface production rates were determined with the CRONUS online calculator (Balco et al., 2008) and are 12.17 at/g/yr and 0.266 at/g/yr for spallation and muons, respectively. The total ^{9}Be represents the carrier and natural ^{9}Be of the samples (ICP-AES measurements). AMS analysis calibration was performed with a BeO NIST 4325 standard at ASTER. ^{10}Be/^{9}Be are blank corrected values. Uncertainties include AMS analysis, carrier mass and blank uncertainties.

Sample	Depth (cm)	Integrated density (g/cm^3)	Mass of quartz (g)	Total ^{9}Be (mg)	^{10}Be/^{9}Be	± (%)	In situ ^{10}Be (at/g quartz)	± (%)
STR11-3	7	0.88	25.02	0.477	1.47E−13	3.1	188144	3.5
STR13-43	22.5	1.19	17.23	0.285	1.55E−13	3.4	171954	3.9
STR13-45	32.5	1.20	19.72	0.293	1.65E−13	4.0	163601	4.5
STR13-47	42.5	1.27	14.68	0.290	1.16E−13	3.9	153162	4.4
STR13-49	52.5	1.34	22.54	0.287	1.70E−13	3.9	144995	4.4
STR13-51	62.5	1.41	18.60	0.277	1.32E−13	3.3	131079	3.9
STR13-53	72.5	1.49	23.79	0.281	1.45E−13	3.8	114030	4.3
STR13-55	82.5	1.56	22.03	0.252	1.23E−13	3.2	97672	3.7
STR13-59	102.5	1.73	22.45	0.303	8.75E−14	3.9	78918	4.4
STR13-61	112.5	1.80	18.32	0.274	6.39E−14	4.0	63992	4.5
STR13-42B	135	1.96	29.31	0.291	8.49E−14	3.9	56360	4.4
STR13-43B	145	2.01	40.35	0.248	1.09E−13	5.2	44712	5.5
STR13-45B	165	2.09	38.00	0.278	7.48E−14	4.5	36532	4.9
STR13-47B	185	2.16	48.84	0.268	8.31E−14	3.9	30440	4.4
STR13-49B	205	2.21	57.09	0.280	8.55E−14	3.8	28057	4.3

For the ^{238}U–^{234}U–^{230}Th–^{226}Ra system, this leads to the following equations:

$$\frac{d^{238}\mathrm{U}}{dt} = f_{238}{}^{238}\mathrm{U}_0 - k_{238}{}^{238}\mathrm{U} - \lambda_{238}{}^{238}\mathrm{U} \quad (1)$$

$$\frac{d^{234}\mathrm{U}}{dt} = f_{234}{}^{234}\mathrm{U}_0 + \lambda_{238}{}^{238}\mathrm{U} - k_{234}{}^{234}\mathrm{U} - \lambda_{234}{}^{234}\mathrm{U} \quad (2)$$

$$\frac{d^{230}\mathrm{Th}}{dt} = f_{230}{}^{230}\mathrm{Th}_0 + \lambda_{234}{}^{234}\mathrm{U} - k_{230}{}^{230}\mathrm{Th} - \lambda_{230}{}^{230}\mathrm{Th} \quad (3)$$

$$\frac{d^{226}\mathrm{Ra}}{dt} = f_{226}{}^{226}\mathrm{Ra}_0 + \lambda_{230}{}^{230}\mathrm{Th} - k_{226}{}^{226}\mathrm{Ra} - \lambda_{226}{}^{226}\mathrm{Ra} \quad (4)$$

where λ_i, k_i and f_i are the radioactive decay, loss and gain constants (in yr^{-1}), respectively, for the radionuclides i (i.e., ^{238}U, ^{234}U, ^{230}Th and ^{226}Ra). In the equations, t is the time elapsed between the reference weathering state and its current state. For simplification during the equation-solving procedure, the input fluxes are expressed as a proportion of the number of atoms of nuclides added per year to the initial sample. The loss (k) and gain (f) terms used in the equations are usually assumed to be constant with time for the purpose of simplicity and tractability (e.g., Dequincey et al., 2002; Dosseto et al., 2008; Ma et al., 2010; Chabaux et al., 2013). The mean production rate of regolith, P (in mm/kyr), can be estimated through the resolution of the above equation system and the determination of the age Δt (in kyr) of a sample relative to a reference sample from deeper in the profile at a distance Δh (in mm) along the weathering direction. For isovolumetric weathering, P is given by the following equation:

$$P = \frac{\Delta h}{\Delta t} \quad (5)$$

As the gain and loss coefficients in equations (1)–(4) are not known and the ^{238}U–^{234}U–^{230}Th–^{226}Ra analyses yield only three independent data per sample, namely the (^{234}U/^{238}U), (^{230}Th/^{234}U) and (^{226}Ra/^{230}Th) ratios, the analysis of only one sample (in addition to a reference sample) is not sufficient to determine the weathering production rate P. The mathematical formalism developed to retrieve such time information assumes that the gain and loss coefficients (k_i and f_i) of the model can be considered constants, at least for a part of the profile from which several different samples can be collected and analyzed. The measured (^{234}U/^{238}U), (^{230}Th/^{234}U) and (^{226}Ra/^{230}Th) ratios of each sample are used to

determine the mobility parameters of the model and the age of different samples relative to the reference sample. The numerical solutions are obtained using a stochastic quantum particle swarm optimization scheme (more details in Chabaux et al., 2013), which minimizes the sum of the squared differences between the measured and estimated activity ratios. The parameter solutions that allow the model to fit the observed activity ratios within 1% error are retained and averaged to obtain a set of optimized output parameter values. The uncertainties in the parameter estimates are calculated as two-sigma standard deviations on the mean parameter estimate. It is important to stress here that such modeling approaches only give mean long-term values, i.e., over several kyr or 10 kyr, for nuclide gain and loss parameters and regolith production rates.

4.2. Regolith denudation rate from in situ ^{10}Be depth profile

As with U-series disequilibrium methodology for regolith production rate, the depth variations of in situ ^{10}Be concentrations within a weathering profile are recognized as a powerful approach to constrain geomorphologic parameters, including the mean denudation rate of a regolith (e.g., Siame et al., 2004; Dosseto and Schaller, 2016). In situ ^{10}Be is produced at the surface of the Earth by the interaction of cosmic rays and rock atomic nuclei (Brown et al., 1995). By taking into account (1) the different attenuation lengths of secondary neutrons and muons, which produce ^{10}Be mainly in surface horizons for neutrons and at greater depths for muons (Kim and Englert, 2004), and (2) their relative contribution to the total produced ^{10}Be, the depth variations of in situ ^{10}Be concentrations within a weathering profile are given by (e.g., Siame et al., 2004; Braucher et al., 2009):

$$\begin{aligned} C(t,d,z) = {} & C_0 \exp(-\lambda t) \\ & + \frac{P_0 * P_n}{\frac{\rho d}{K_n} + \lambda} \exp\left(\frac{-\rho z}{K_n}\right)\left(1 - \exp\left(-t\left(\frac{\rho d}{K_n} + \lambda\right)\right)\right) \\ & + \frac{P_0 * P_{nm}}{\frac{\rho d}{K_{nm}} + \lambda} \exp\left(\frac{-\rho z}{K_{nm}}\right)\left(1 - \exp\left(-t\left(\frac{\rho d}{K_{nm}} + \lambda\right)\right)\right) \\ & + \frac{P_0 * P_{fm}}{\frac{\rho d}{K_{fm}} + \lambda} \exp\left(\frac{-\rho z}{K_{fm}}\right)\left(1 - \exp\left(-t\left(\frac{\rho d}{K_{fm}} + \lambda\right)\right)\right) \end{aligned} \quad (6)$$

where t is the exposure age of the profile (in yr), d is the mean denudation rate (in cm/yr), z is the depth of each sample (in cm), C_0 is the initial concentration from previous exposure (in atoms/g quartz), λ is the radioactive decay of the ^{10}Be (in yr^{-1}) and ρ is the integrated density of each sample (in g/cm^3). P_0 is the total production rate of ^{10}Be at the surface of the soil (12.17 at/g/yr and 0.266 at/g/yr for spallation and muons, respectively, determined with the CRONUS online calculator; Balco et al., 2008). P_n, P_{nm} and P_{fm} are the relative contributions of 97.85, 1.5 and 0.65% to the total production and K_n, K_{nm} and K_{fm} are the effective attenuation lengths of 150, 1500 and 5300 g/cm^2, for secondary neutrons, negative muons and fast muons, respectively (Braucher et al., 2009). The depth variations of in situ ^{10}Be concentrations in a weathering profile can thus be used to estimate the exposure age and the mean denudation rate of a regolith, in addition to the inherited ^{10}Be concentration, without any steady state assumption.

4.3. Chemical mobility and volumetric variation

In addition to the determination of regolith production and denudation rates from the above approaches, the chemical mobility and volumetric variation associated with the weathering processes can be estimated through the analysis of major and trace element concentrations. Based on the presence of an immobile element j, the chemical mobility of an element i during weathering can be quantified by mass transfer coefficients (Brimhall et al., 1991), as defined by the following:

$$\tau_i = \left(\frac{C(i)_{sample} * C(j)_{bedrock}}{C(i)_{bedrock} * C(j)_{sample}} - 1\right) \quad (7)$$

where $C(i)_{sample}$ and $C(i)_{bedrock}$ represent the concentrations of the element i for a given sample and for the deepest bedrock sample and $C(j)_{sample}$ and $C(j)_{bedrock}$ represent the concentrations of the immobile element j for a given sample and for the deepest bedrock sample, respectively. Positive or negative τ_i values imply the gain or loss, respectively, of the element i relative to the deepest bedrock sample, taken here as the reference rock. In addition, the chemical depletion fraction (Riebe et al., 2003), allows an estimation of the denudation fraction due to chemical weathering between the reference bedrock sample and a given sample and is defined by the following:

$$CDF = \left(1 - \frac{C(j)_{bedrock}}{C(j)_{sample}}\right) \quad (8)$$

It is also possible to estimate the relative volume variation associated with rock weathering between two considered levels by the volumetric strain index calculation (Brimhall et al., 1991; Riebe et al., 2003):

$$\varepsilon = \left(\frac{C(j)_{bedrock} * d_{bedrock}}{C(j)_{sample} * d_{sample}}\right) - 1 \quad (9)$$

where $d_{bedrock}$ and d_{sample} are the bulk density values of the bedrock and the considered sample, respectively. Values of ε close to zero imply isovolumetric weathering, while positive or negative values indicate expansion or compaction, respectively.

5. Results

5.1. Mineralogical and geochemical variations within the weathering profile

The whole rock XRD analyses are presented in Electronic Supplement and in Table ES1. These data along with the thin section observations are consistent with previously published data for the Strengbach site (e.g., Fichter et al., 1998) and indicate that quartz and muscovite do not present any significant evidence of weathering in the granitic bedrock. Biotite is weathered at all depths and replaced by clays, sericite and hematite. The K-feldspar and plagioclase crystals show structural and mineralogical evolution from the base to the top of the granite, with a higher density of clay filled cracks in samples from the granite top. Carlsbad and polysynthetic twins are identifiable at the granite base, while it is more difficult to recognize them at the granite top. The analysis of the <2 µm clay fraction indicates that the clay composition is relatively homogeneous within the granitic bedrock and is dominated by illite (40 to 60% illite, 20 to 30% inter-stratified illite/smectite, 5 to 25% of smectite and 5 to 10% of kaolinite). The clay composition is different and more variable in the soil, where the smectite and inter-stratified clays become dominant (60 to 70%) followed by the illite (20 to 30%) and kaolinite (5 to 10%). These data show a significant increase in supergene alteration from the base to the top of the profile, in accordance with the increase in the loss on ignition (LOI, Table 1).

The variations in the major and trace element concentrations within the weathering profile (Table 1) have been used to estimate

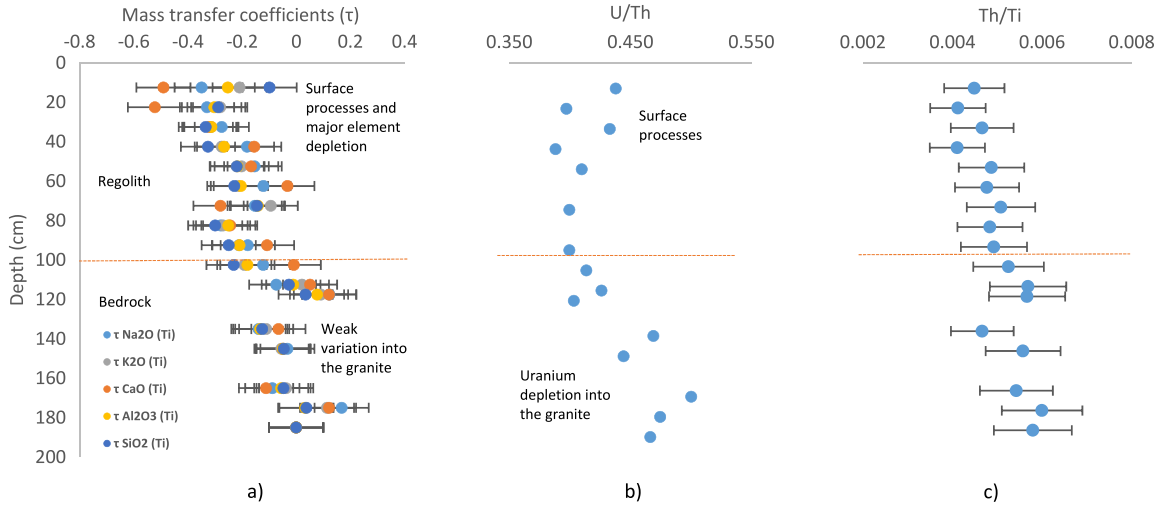

Fig. 2. a) Mass transfer coefficients calculated from equation (7). The uncertainty is calculated from elemental concentration uncertainty propagation and is <20% (error bars show 20% level). b) U/Th ratio. The U and Th concentrations are calculated from isotopic dilution. The uncertainty is 0.2% for U, 0.5% for Th and is within size point. c) Th/Ti ratio. The Ti and Th concentrations are calculated from alkaline fusion. The uncertainty is <15% (error bars show 15% level).

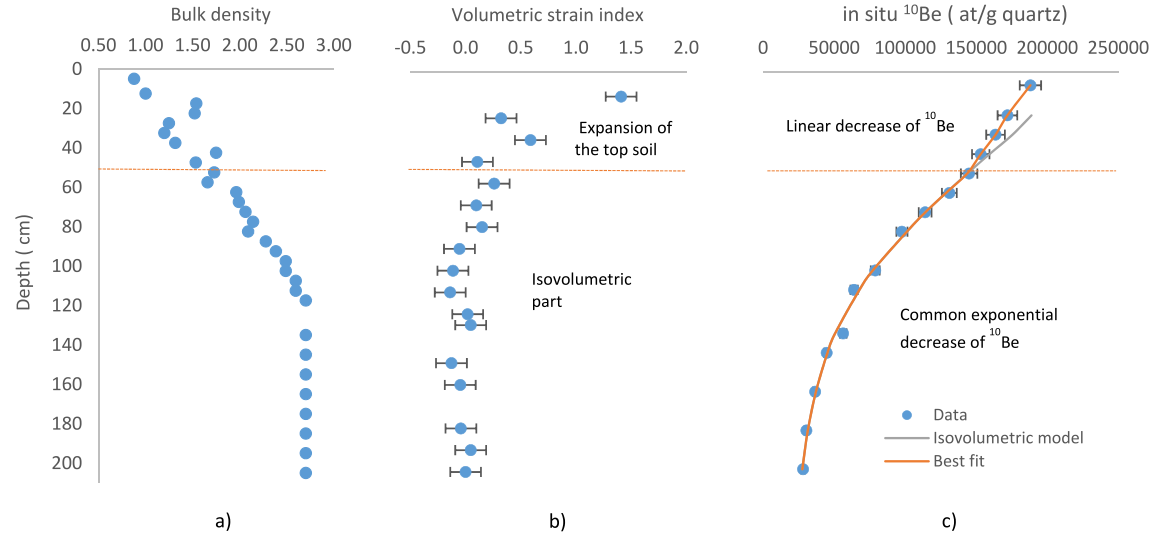

Fig. 3. a) Bulk density calculated by combining the fine fraction density and the density of blocks with respect to the proportion of blocks in each horizon. For the bedrock and the blocks of granite, a constant density of 2700 kg/m^3 is assumed. b) Volumetric strain index calculated from equation (9). Uncertainty is calculated from elemental concentration uncertainty propagation and is <10% (error bars show 10% level). c) ^{10}Be depth profile. In blue: measured ^{10}Be concentrations. Uncertainty is <5% (error bars show 5% level). In red: best fit obtained from optimization by Levenberg–Marquardt algorithm. In grey: modeled ^{10}Be concentrations without taking into account soil expansion. (For interpretation of the references to color in this figure legend, the reader is referred to the web version of this article.)

the chemical mobility associated with weathering by the calculation of the mass transfer coefficients. For this calculation, Ti is often considered one of the best-suited immobile elements (e.g., Egli et al., 2006). For the tau calculation, the normalization to Ti rather than to Zr concentration has been preferred, even if Zr can be considered immobile in such environment (Rihs et al., 2011). The reason is the better analytical precision obtained for the Ti concentrations (3%) than for Zr (≈10%), which leads to a better precision of the tau values determined with Ti (≈10%) than with Zr (≈20%). The calculation of relatively constant ratios within the profile between Ti and other elements usually considered immobile, such as Ta (not shown) and Th (Fig. 2c), especially in the deeper part of the profile, reinforces the assumption that Ti is mainly immobile during weathering. Tau values indicate no significant mobility for the main major elements (Na_2O, K_2O, CaO, Al_2O_3, and SiO_2) in the deeper part of the granitic profile below 100 cm depth (Fig. 2a). The depletion becomes significant in the regolith portion above 100 cm depth, with chemical mobility trends that differ from one element to another, especially in the uppermost part of the soil known to be significantly affected by biological processes, vegetation cycling and atmospheric deposition (e.g., Stille et al., 2011; Gangloff et al., 2014). In this upper part of the profile, the volumetric strain index indicates a significant expansion of the soil horizons, with ε values from 50 to 150%, while deeper in the profile, in the granite and saprolite horizons, the weathering is nearly isovolumetric (Fig. 3b).

As for tau values, the depth variations in the U/Th concentration ratios measured by isotopic dilution, which are more precisely estimated than the tau values, allow for subdividing the profile into two main zones, with U loss in the lower part of the profile, which gradually decreases upwards up to approximately a depth of 100 cm, and a U/Th ratio increase toward the surface above 100 cm (Fig. 2b). This increase might indicate Th migration due to complexation with organic colloids, as observed at other sites (Rihs et al., 2011), or U inputs from external atmospheric deposition, as suggested in other contexts (Pelt et al., 2013; Chabaux et al., 2013). Regardless of the precise origin of this increase, the U/Th data confirm that the transition between granitic

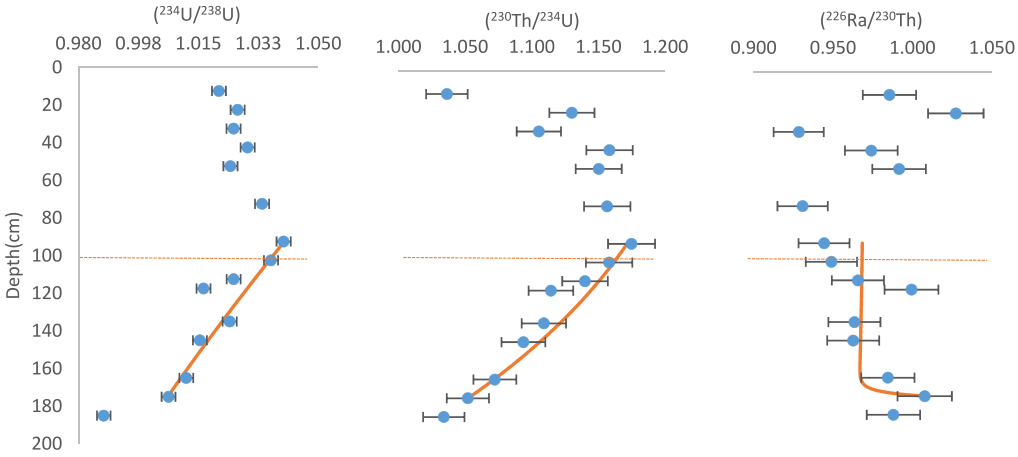

Fig. 4. ($^{234}U/^{238}U$), ($^{230}Th/^{234}U$) and ($^{226}Ra/^{230}Th$) radioactive activity ratios along the weathering profile. In blue: experimental data. The uncertainties are at the 2σ level: 0.2% for ($^{234}U/^{238}U$), 1.5% for ($^{230}Th/^{234}U$) and 1.7% for ($^{226}Ra/^{230}Th$) measured activity ratios. In red: best fit obtained from numerical optimization. Calculated coefficients: $k_{238} = 4.81 \times 10^{-6} \pm 3.68 \times 10^{-7}$, $k_{234} = 5.47 \times 10^{-6} \pm 9.20 \times 10^{-7}$, $k_{226} = 2.22 \times 10^{-5} \pm 4.44 \times 10^{-6}$, $f_{238} = 1.63 \times 10^{-6} \pm 4.00 \times 10^{-7}$, $f_{234} = 2.76 \times 10^{-6} \pm 8.96 \times 10^{-7}$ and $f_{226} = 6.61 \times 10^{-6} \pm 2.20 \times 10^{-6}$ (2σ level, expressed in yr^{-1}). Calculated weathering age is approximately 69,000 yr for the modeled section. (For interpretation of the references to color in this figure legend, the reader is referred to the web version of this article.)

bedrock and regolith at a depth of approximately 100 cm vertically divides the weathering profile into two distinct zones that are marked by different chemical mobility values and likely exhibit specific weathering processes.

5.2. U–Th–Ra and in situ ^{10}Be systematics

The depth subdivision of the profile inferred from major and trace element mobility is also observed in the U–Th–Ra disequilibrium data (Table 2, Fig. 4). The lower part of the profile (below 100 cm depth) is characterized by rather simple and continuous variation trends in the ($^{234}U/^{238}U$), ($^{230}Th/^{234}U$) and ($^{226}Ra/^{230}Th$) activity ratios with depth, with an increase in the ($^{234}U/^{238}U$) and ($^{230}Th/^{234}U$) ratios with decreasing depth and a decrease in the ($^{226}Ra/^{230}Th$) ratios with decreasing depth (Fig. 4). In the upper regolith, the ($^{234}U/^{238}U$) and ($^{230}Th/^{234}U$) activity ratios define clearly opposite trends with depth, which support the suggestion that the two parts of the profile are marked by different weathering processes. The upper part of the profile is also characterized by much more scattered ($^{226}Ra/^{230}Th$) ratios, without a simple correlation with depth.

For in situ ^{10}Be, the concentrations point to a progressive decrease with depth but with two different patterns of variation in the profile, one in the deeper horizons, where the weathering is isovolumetric, and the second one in the uppermost regolith horizons (<50 cm), which are affected by volumetric expansion (Table 3, Fig. 3). The deeper part is characterized by a common exponential decrease in ^{10}Be, while the soil to upper regolith part (0–50 cm) is characterized by a linear decrease in the in situ ^{10}Be concentration with depth (Fig. 3).

6. Discussion

6.1. Determination of regolith production and denudation rates

The mineralogical and geochemical data lead to a depth-dependent division of the profile into two main parts, with progressive variation trends of the U-series systematic in the bedrock and more scattered variations in the upper horizons (Fig. 4). Similar to the results of the analyses of the short half-life ^{228}Ra and ^{228}Th nuclides in soil profiles from different forest catchments, including the Strengbach (Rihs et al., 2011; Gontier et al., 2015), the short-distance variations in the upper horizons most likely result from preferential Th mobility related to the differential mobilization of radionuclides in the presence of organic matter. As also emphasized in Gontier et al. (2015), such short-distance redistributions in the soil horizons may imply significant variability of the mobility coefficients in this part of the profile, at least for Th isotopes. Thus, this effect prevents the direct application of the radioactive disequilibrium methodology described in section 4.1. In the Strengbach case, and likely in many other forest contexts, the bedrock is thus the most suitable place to quantify the mean long-term regolith production rate via the conventional U–Th–Ra methodology. In the present study, the modeling approach has been therefore applied only to the lower part of the profile, in which Th can be assumed to be immobile (Fig. 2c), consequently reducing the number of unknowns in the modeling ($k_{230} = 0$ and $f_{230} = 0$). The modeling results (Fig. 4) show that the mean U mobility parameters fall within the range of existing data for shale and granodiorite lithologies (Ma et al., 2010; Dequincey et al., 2002; Dosseto et al., 2008; Chabaux et al., 2013). As evidenced by the obtained coefficients, the particular positive correlation between ($^{234}U/^{238}U$) and ($^{230}Th/^{234}U$) ratios in the deeper part of the profile do not correspond to a simple leaching of U. To explain the ratios of ($^{234}U/^{238}U$)>1 and ($^{230}Th/^{234}U$)>1, U removal must have occurred at a higher rate than U input, and incoming U, which may originate from U mobilization in the upper horizons, must have been characterized by a higher ^{234}U–^{238}U fractionation than the removed U (Fig. 4, details also in Dequincey et al., 2002). Such mobility implies precipitation of U-rich secondary minerals, such as Fe-oxyhydroxides, from fluids with ratios of ($^{234}U/^{238}U$)>1. This hypothesis is supported by the ratios of ($^{234}U/^{238}U$)>1 in soil solutions from a neighboring profile in the same part of the watershed (Prunier et al., 2015). The U–Th–Ra modeling also gives the elapsed time between the granite base and the lower regolith, which yields a mean regolith production rate of 12 ± 4 mm/kyr. Considering the density of 2.5 for the lower regolith, the regolith production rate in terms of specific flux is 30 $\pm$ 10 T/km^2/yr.

For application of the in situ ^{10}Be approach (section 4.2), a numerical inverse procedure has been used to determine the exposure age, the mean denudation rate and the inherited concentration that best explain the data from equation (6). The inverse procedure consists of minimizing the chi-square value of the system by the algorithm of Levenberg–Marquardt (Marquardt, 1963) and has been adapted to take into account the volumetric expansion of the upper regolith. The chi-square value is defined as follows:

Table 4
Synthesis table of the studied sites that allow for U-series and ^{10}Be results comparison. When rates are not provided in T/km^2/yr, conversions from mm/kyr to T/km^2/yr have been performed by assuming a regolith bulk mean density of 1700 kg/m^3. (1) This study. (2) Cotel et al. (2016). (3) Ma et al. (2010). (4) West et al. (2013). (5) Jin et al. (2010). (6) Schoonejans et al. (2016). (7) Dosseto et al. (2008). (8) Heimsath et al. (2000). (9) Chabaux et al. (2013). (10) Brown et al. (1995). (11) McDowell and Asbury (1994). ^{10}Be denudation rates have been determined by in situ ^{10}Be data, except for West et al., 2013, where meteoritic ^{10}Be has been used.

Site	Regolith production from U-series data (T/km^2/yr)	Regolith denudation from profile ^{10}Be data (T/km^2/yr)	Regolith denudation from river sediment ^{10}Be data (T/km^2/yr)	Erosion from river sediment load (T/km^2/yr)
Strengbach Catchment (France)	$30 \pm 10_{(1)}$	$37 \pm 15_{(1)}$	–	$10 \pm 2_{(2)}$
Susquehanna Shale Hills Observatory (United States)	29 ± 24–$77 \pm 20_{(3)}$	27 ± 10–$34 \pm 10_{(4)}$	$39_{(5)}$	–
Betic Range (Spain)	12 ± 2–$41 \pm 9_{(6)}$	24 ± 5–$39 \pm 3_{(6)}$	–	–
Nunnock Catchment (Australia)	20 ± 3–$130 \pm 24_{(7)}$	12 ± 2–$90 \pm 5_{(8)}$	$87 \pm 9_{(8)}$	–
Rio Icacos Watershed (Porto Rico)	$76 \pm 20_{(9)}$	42 ± 15–$85 \pm 30_{(10)}$	$73 \pm 25_{(10)}$	$300_{(11)}$

$$X = \sum \left(\frac{C_{data}(z) - (C_{model}(t, d, C_0, z) + \Delta C)}{\sigma(z)} \right)^2 \quad (10)$$

where $C_{data}(z)$ and $C_{model}(t, d, C_0, z)$ are the measured and modeled ^{10}Be concentrations, respectively, and $\sigma(z)$ is the uncertainty in the measured ^{10}Be concentration for a sample at depth z. A correction factor ΔC has been introduced to take into account the volumetric expansion of the upper 50 cm because the density variation only is insufficient to explain the concentration trend of this part of the profile. This implies that expansion must have occurred relatively late (<5–10 kyr) in the history of the profile, as the measured concentrations do not reflect the corresponding production rate changes. Uncertainty in the parameters is estimated from the covariance matrix of the problem. It is important to stress that, considering the mean denudation and the surface ^{10}Be production rates at the summit of the Strengbach watershed, the current accumulation of ^{10}Be within the profile is not balanced by erosion and radioactive decay. Because a ^{10}Be concentration steady state is not present, the geochronometric application of the modeling is possible. The best fit gives an exposure age of the profile of 19,734 ± 2,168 yr, a mean denudation rate of 22 ± 10 mm/kyr (in terms of specific flux, 37 ± 15 T/km^2/yr, based on the mean density of the regolith of 1.7) and an inherited ^{10}Be concentration of 15,000 ± 1,000 at/g quartz (Fig. 3).

6.2. Implications for regolith evolution on the millennial timescale

To the best of our knowledge, this study is likely the first one to combine U-series and in situ ^{10}Be analyses on the same samples in a single weathering profile with such a depth extent and spatial resolution. This coupled approach allows for determining, in addition to the regolith denudation and production rates, the exposure age of the profile and the potential ^{10}Be inherited concentration. As illustrated in the following, these estimates are relevant for recovering the Quaternary dynamics of the weathering profile.

The determined exposure age inferred from the ^{10}Be data indicates the occurrence of an erosive event at the summit of the Strengbach watershed approximately 20,000 yr ago, likely resulting from glacial or peri-glacial processes in relation with the last Würm glaciation, which is in accordance with regional investigations (Seret et al., 1990; Mercier et al., 1999). In addition, the occurrence of an inherited ^{10}Be concentration within the bedrock indicates a complex erosive history at the summit of the Strengbach catchment. By extrapolating the long-term regolith propagation rate determined from U–Th–Ra variations (i.e., 30 ± 10 T/km^2/yr or 12 ± 4 mm/kyr), an age of approximately 150 kyr is obtained for the entire 2 m-thick profile analyzed in this study. This age would lead to a ^{10}Be concentration at 2 m depth much higher than the inherited ^{10}Be concentration of 15,000 at/g quartz obtained from our data. In this bedrock, the measured inherited ^{10}Be concentration corresponds to the concentration obtained from a muonic exposure at approximately 4 m depth over ≈150 kyr. A way to reconcile all the data, assuming the above determined average denudation rate of 22 mm/kyr, is that a thickness of 2 m was eroded 20 kyr ago and that a total resetting of the bedrock ^{10}Be inventory must have occurred 150 kyr ago, which is consistent with the fact that the penultimate Riss glaciation was probably more intense than the last Würm glaciation in the mountains of central Europe (Dehnert et al., 2010).

The independent determination of regolith production and denudation rates from U–Th–Ra isotopes and in situ ^{10}Be constitutes an interesting method for discussing the stability state of a weathering profile on a millennial timescale. For the Strengbach case, the proposed approach gives similar values for denudation rate (37 ± 15 T/km^2/yr) and production rate (30 ± 10 T/km^2/yr), suggesting that at a millennial time scale, the regolith mass balance at the summit of the catchment is close to steady state, even if it was perturbed 20 kyr ago. Such a conclusion may indicate that the return to mass balance steady state is relatively fast in this system, i.e., obtained in less than 20 kyr and/or that the erosive event that occurred 20 kyr ago has only transiently disturbed the processes controlling regolith formation at the summit of the Strengbach watershed. The results may also suggest that the recent anthropogenic perturbations linked to the 20th century, e.g., acid rain or the recent afforestation efforts, which may have recently modified the cationic concentrations and acidity of soil and stream waters in the watershed (Viville et al., 2012; Prunier et al., 2015), have not perturbed the ^{10}Be and U–Th–Ra long-term records.

Very few other studies combining U-series disequilibrium and cosmonuclides methodology exist for other sites, even when including those involving the meteoritic ^{10}Be approach (Table 4). In addition, these other studies usually dealt with more superficial regolith and different sample sets for isotopic analyses. However, despite these limitations, the data indicate that in all the investigated mid-mountain catchments, which are characterized by different climatic and tectonic settings, there is a fairly good consistency between the long-term regolith production and denudation rates (Table 4). This seems to be especially true at the ridge-tops and/or hill-crests of watersheds, where geochronological interpretations are likely less affected by colluvial transport and deposition. Altogether, even if such a conclusion remains preliminary, the current data suggest that the long-term regolith evolution could be commonly at steady state.

6.3. Comparison of millennial and present-day weathering and erosion rates

Because U-series and ^{10}Be approaches integrate long-term processes, a substantial step to understand the recent regolith evolution could be provided by the comparison of long-term weathering and erosion rates with present-day estimates. As established by Riebe et al. (2003), the knowledge of denudation rates determined by cosmogenic nuclide, combined with the geochemical mass balance approaches and the definition of the chemical depletion fraction (CDF), allow to distinguish the chemical and physical components of the total denudation. This approach is predicated

on an assumption of steady state, which is supported by the consistency between U-series and ^{10}Be results. The total weathering rate in T/km^2/yr is as follows:

$$W = D\left(1 - \frac{C(\mathrm{Ti})_{rock}}{C(\mathrm{Ti})_{soil}}\right) = D \times CDF \quad (11)$$

where D is the mean denudation rate in T/km^2/yr inferred from the cosmogenic ^{10}Be and $C(\mathrm{Ti})_{rock}$ and $C(\mathrm{Ti})_{soil}$ are the concentrations of titanium (considered an immobile element) in the bedrock and in the soil, respectively. The application of this approach to the bedrock and the soil levels of the studied weathering profile leads to a CDF value of 0.22 when using for the average Ti concentrations of the bedrock and soil levels. A maximum CDF value of 0.30 is obtained by using the lowest Ti concentrations measured in the bedrock and the highest concentrations in the soil. Similar calculations can be made with Zr, which can also be considered an immobile element in the Strengbach catchment (Rihs et al., 2011): CDF values between 0.13 and 0.25 are obtained according to whether the average concentration values or the extreme values are used for each level. These different calculations indicate that at the profile scale, long-term chemical weathering accounts for 13 to 30% of the total denudation, which yields a long-term chemical weathering flux of between 5 and 11 T/km^2/yr and consequently a long-term erosion flux of between 26 and 32 T/km^2/yr. Therefore, physical erosion is the main process controlling the loss of regolith.

The above weathering flux calculations can be easily adapted to calculate the long-term weathering flux of a specific chemical element by using the mean denudation rate (D), the elemental concentrations within the bedrock ($C(x)_{bedrock}$) and the tau values (τ_x) in the upper soil (Riebe et al., 2003):

$$W_x = D * C(x)_{bedrock} * (-\tau_x) \quad (12)$$

Based on this approach, long-term weathering fluxes of approximately 3 $\pm$ 2 T/km^2/yr for Si and 0.7 $\pm$ 0.47 T/km^2/yr for cations can be estimated from the geochemical variations along the regolith profile at the watershed summit. Similarly, the regular analyses of the dissolved fluxes and the sediment loads carried by the Strengbach stream allow for estimation of the current erosion and weathering rates at the watershed scale. The combination of the suspended and bed load monitoring yields a total erosion rate of 5 $\pm$ 1 T/km^2/yr at the watershed outlet (Viville et al., 2012). By correcting the net flux for basic cations from atmospheric deposition, a cationic weathering flux of 1.98 $\pm$ 0.2 T/km^2/yr and a Si weathering flux of 2.89 $\pm$ 0.3 T/km^2/yr are estimated (Viville et al., 2012). The current exported flux for Si determined at the watershed outlet is surprisingly very close to the long-term Si weathering flux associated with regolith formation inferred for the watershed summit. This consistency means that the first-order chemical weathering, which is controlled by the rates of primary mineral dissolution and secondary mineral precipitation, is rather spatially uniform and stable in time. In contrast, the current cationic flux in the Strengbach stream seems to be higher than the long-term flux determined at the profile scale for basic cations. This difference may be due to a recent increase in basic cation leaching from Strengbach soils, possibly triggered by the acidic atmospheric inputs and/or the forest management evolution experienced by the Strengbach catchment in recent decades (Viville et al., 2012; Prunier et al., 2015). In contrast to the weathering rates, the long-term erosion rate determined from ^{10}Be and CDF data (approximately 30 T/km^2/yr) is clearly higher than the current erosion rate determined in the Strengbach stream (approximately 5 T/km^2/yr; Viville et al., 2012). The latter value is certainly an underestimate, as the suspended load was sampled only once every one or two weeks, which probably does not allow for a correct estimate of the suspended load exported during flood events. A more recent study of the erosion fluxes exported from the Strengbach watershed at its outlet, including an accurate determination of the suspended load exported from the watershed during flood events, yielded an erosion rate no higher than 10 T/km^2/yr (Cotel et al., 2016). Regarding the sampling frequency developed in the latter study, and even if the bed load is always difficult to estimate precisely, an additional bias for the current erosion rates by a factor of three seems improbable. Thus, unlike weathering fluxes, the long-term erosion rate determined at the watershed summit and the present-day rate at the watershed scale are most likely different. Such a discrepancy is certainly not surprising, and can result from spatial heterogeneity in the erosion rate at the watershed scale, with high erosion rates along the main crests possibly counterbalanced by sediment storage downhill. It could also result from temporal variability in the physical erosion rate, with, for instance, high erosion rates during cold conditions, probably persisting long after the LGM, followed by lower erosion rates due to stabilization of the regolith by soil and vegetation cover development during the Holocene.

As illustrated in the Strengbach case, this combination of U-series, in situ ^{10}Be and stream monitoring allows for discussing the weathering and erosion variability at different spatial and temporal scales. Another site where a similar comparison is possible is the Rio Icacos watershed (Table 5 in Chabaux et al., 2013). Similar to the Strengbach catchment, the data from the Rio Icacos watershed suggest relatively similar long-term and short-term weathering rates, and also significant differences between denudation rates inferred from ^{10}Be data and current erosion rates determined from sediment monitoring (Table 4). However, in this case, unlike the Strengbach catchment, the current erosion rates are higher than the long-term ones. This large variability in the physical erosion fluxes through time is also suggested in a few other studies. In the Susquehanna Shale Hills Observatory, it has been proposed that current erosion rates may be lower than previous conditions because deep sediments in the valley floor appear to retain a record of enhanced colluvial transport in the past (West et al., 2013). In Australia, longer sediment residence times have been proposed for the Murrumbidgee River during warm periods, in association with the development of vegetation cover and a decrease in erosion (in Dosseto and Schaller, 2016). Even if, once again, there are very few sites where long-term trends are compared to short-term trends, it seems that mid-mountain watersheds that experienced glacial or periglacial conditions during the LGM (Strengbach, SSHO or Australian upper watersheds) recorded a decrease in erosion rates with the onset of Holocene. In contrast, in the Rio Icacos watershed, characterized by warmer conditions and hence unaffected by periglacial processes, the current erosion rates are faster (Table 4). Thus, the above data support the assumption deduced from the Strengbach case that the erosion rates have been more variable than the chemical weathering rates during the Quaternary. The data might also suggest a possible role of periglacial processes in the erosional response to Quaternary climatic variations.

7. Conclusions

The study performed on a weathering profile sampled at the summit of the Strengbach catchment illustrates the interesting results of the combined analyses of in situ ^{10}Be concentrations, ^{238}U–^{234}U–^{230}Th–^{226}Ra disequilibria and major and trace element concentrations. As summarized in Fig. 5, this combination is a powerful methodology for recovering key parameters of the long-term regolith evolution. This approach suggests that the long-term regolith evolution in the Strengbach watershed is relatively close to steady state, despite recent anthropogenic perturbations. In addition, in regard to the mineralogical properties of the profile and

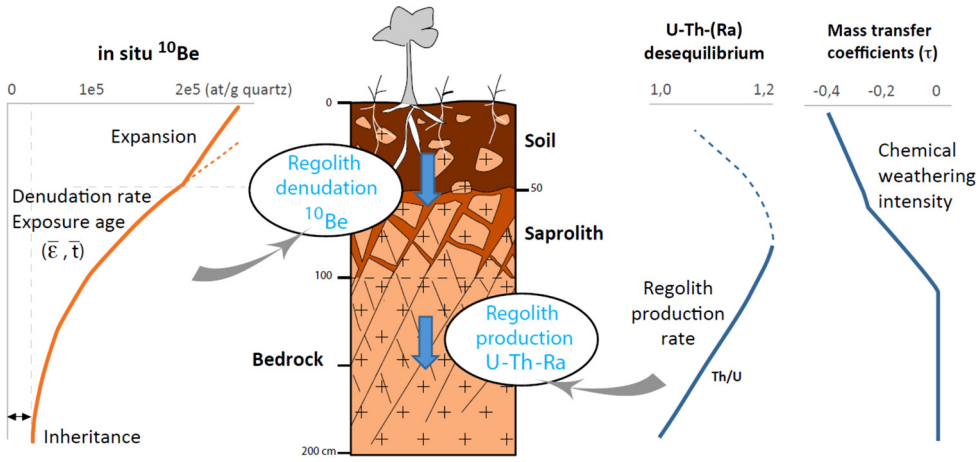

Fig. 5. Summary of the methodologies applied to the regolith profile at the Strengbach catchment summit. Combined approaches allow for constraining the long-term evolution of the profile with comparison of both regolith production and denudation rates.

implicit assumptions of the U–Th–Ra modeling, it appears that in this site (and lakely in many other forest contexts), the bedrock is the most suitable place to quantify the regolith production rate using the U–Th–Ra methodology. The results also highlight the importance of having a sufficiently dense sampling strategy along the regolith depth profile to recover the Quaternary polyphase history of the regolith from the analysis and modeling of in situ ^{10}Be. In combination with the above data, geochemical and mass balance calculations performed in the Strengbach stream and along the weathering profile allow for investigating the regolith evolution at different spatial and temporal scales. The results indicate that physical erosion is the dominant process of regolith loss in the Strengbach catchment and has probably varied much more than chemical weathering through time. Although very few sites with U-series, in situ ^{10}Be and stream monitoring data are available for comparison, the current data suggest that (1) mass balance steady state of regolith can be commonly achieved in soil mantled landscapes, and (2) physical erosion has exhibited higher variability than chemical weathering over the last 10–150 kyr. The combined U-series and in situ ^{10}Be analyses in high spatial resolution depth profiles could become a powerful approach in the future for providing new quantitative insights on weathering profile dynamics and regolith erosive history over Holocene and Late Pleistocene time periods. The association of these approaches with the monitoring of water chemistry and sediment fluxes at watershed outlets seems also important to correctly positioning the present-day erosion and weathering rates relative to the past rates recorded by the U–Th–Ra and in situ ^{10}Be inventories.

Acknowledgements

This work has been supported by the funding of a Ph.D. scholarship to J. Ackerer from the Region Alsace, France and the BRGM, Orléans, France. ^{10}Be ratios were measured at the ASTER AMS national facility (CEREGE, Aix-en-Provence), supported by INSU-CNRS, IRD and CEA. This study was financially supported by funding from the REALISE program to F. Chabaux. We are grateful to A. Aubert and N. Maubec for the X-ray diffraction measurements and interpretations and to R. Boutin for the analysis of the major and trace element concentrations. We also thank M. Granet and T. Perrone for their help during sample preparation and P. Stille, M.C. Pierret and C. Bosia for discussions during the course of the work. We sincerely thank S. Brown and two anonymous reviewers, as well as the Editor D. Vance, for their very constructive and thoughtful comments. This is a LHyGeS-EOST contribution.

Appendix A. Supplementary material

Supplementary material related to this article can be found online at http://dx.doi.org/10.1016/j.epsl.2016.08.005.

References

Akovali, Y.A., 1996. Nuclear data sheets for A = 226. Nucl. Data Sheets 77 (2), 433–470.
Anderson, R.S., Repka, J.L., Dick, G.S., 1996. Explicit treatment of inheritance in dating depositional surfaces using in situ ^{10}Be and ^{26}Al. Geology 24 (1), 47–51.
Balco, G., Stone, J.O., Lifton, N.A., Dunai, T.J., 2008. A complete and easily accessible means of calculating surface exposure ages or erosion rates from ^{10}Be and ^{26}Al measurements. Quat. Geochronol. 3 (3), 174–195.
Banwart, S., Bernasconi, S.M., Bloem, J., Blum, W., Brandao, M., Brantley, S., Zhang, B., 2011. Soil processes and functions in critical zone observatories: hypotheses and experimental design. Vadose Zone J. 10 (3), 974–987.
Brantley, S.L., Goldhaber, M.B., Ragnarsdottir, K.V., 2007. Crossing disciplines and scales to understand the critical zone. Elements 3 (5), 307–314.
Braucher, R., Del Castillo, P., Siame, L., Hidy, A.J., Bourlès, D.L., 2009. Determination of both exposure time and denudation rate from an in situ-produced ^{10}Be depth profile: a mathematical proof of uniqueness. Model sensitivity and applications to natural cases. Quat. Geochronol. 4 (1), 56–67.
Brimhall, G.H., Ford, C., Bratt, J., Taylor, G., Warin, O., 1991. Quantitative geochemical approach to pedogenesis: importance of parent material reduction, volumetric expansion, and eolian influx in lateritization. Geoderma 51 (1), 51–91.
Brocard, G.Y., Van Der Beek, P.A., Bourlès, D.L., Siame, L.L., Mugnier, J.L., 2003. Long-term fluvial incision rates and postglacial river relaxation time in the French Western Alps from ^{10}Be dating of alluvial terraces with assessment of inheritance, soil development and wind ablation effects. Earth Planet. Sci. Lett. 209 (1), 197–214.
Brown, E.T., Stallard, R.F., Larsen, M.C., Raisbeck, G.M., Yiou, F., 1995. Denudation rates determined from the accumulation of in situ-produced ^{10}Be in the Luquillo Experimental Forest, Puerto Rico. Earth Planet. Sci. Lett. 129 (1), 193–202.
Chabaux, F., Riotte, J., Dequincey, O., 2003. U–Th–Ra fractionation during weathering and river transport. Rev. Mineral. Geochem. 52, 533–576.
Chabaux, F., Ma, L., Stille, P., Pelt, E., Granet, M., Lemarchand, D., Brantley, S.L., 2011. Determination of chemical weathering rates from U series nuclides in soils and weathering profiles: principles, applications and limitations. Appl. Geochem. 26, S20–S23.
Chabaux, F., Blaes, E., Stille, P., di Chiara Roupert, R., Pelt, E., Dosseto, A., Brantley, S.L., 2013. Regolith formation rate from U-series nuclides: implications from the study of a spheroidal weathering profile in the Rio Icacos watershed (Puerto Rico). Geochim. Cosmochim. Acta 100, 73–95.
Cheng, H., Edwards, R.L., Hoff, J., Gallup, C.D., Richards, D.A., Asmerom, Y., 2000. The half-lives of uranium-234 and thorium-230. Chem. Geol. 169 (1), 17–33.
Cotel, S., Viville, D., Pierret, M.C., Benarioumlil, S., Chabaux, F., 2016. Evaluation of fluxes of suspended matters and bedload in the small granitic Strengbach catchment (Vosges massif, France). In: Geophysical Research Abstracts, vol. 18. EGU2016-13179.
Cui, L., Liu, C.Q., Xu, S., Zhao, Z.-Q., Liu, T.-Z., Liu, W.-J., Zhang, Z.-J., 2016. Subtropical denudation rates of granitic regolith along a hill ridge in Longnan, SE China derived from cosmogenic nuclides depth-profiles. J. Asian Earth Sci. 117, 146–152.
Dehnert, A., Preusser, F., Kramers, J.D., Akcar, N., Kubik, P.W., Reber, R., Schluechter, C., 2010. A multi-dating approach applied to proglacial sediments attributed to the Most Extensive Glaciation of the Swiss Alps. Boreas 39 (3), 620–632.

Dequincey, O., Chabaux, F., Clauer, N., Sigmarsson, O., Liewig, N., Leprun, J.C., 2002. Chemical mobilizations in laterites: evidence from trace elements and ^{238}U–^{234}U–^{230}Th disequilibria. Geochim. Cosmochim. Acta 66 (7), 1197–1210.

Dosseto, A., Turner, S.P., Chappell, J., 2008. The evolution of weathering profiles through time: new insights from uranium-series isotopes. Earth Planet. Sci. Lett. 274 (3), 359–371.

Dosseto, A., Buss, H., Suresh, P.O., 2012. Rapid regolith formation over volcanic bedrock and implications for landscape evolution. Earth Planet. Sci. Lett. 337, 47–55.

Dosseto, A., Schaller, M., 2016. The erosion response to Quaternary climate change quantified using uranium isotopes and in situ-produced cosmogenic nuclides. Earth-Sci. Rev. 155, 60–81.

Egli, M., Mirabella, A., Sartori, G., Zanelli, R., Bischof, S., 2006. Effect of north and south exposure on weathering rates and clay mineral formation in Alpine soils. Catena 67 (3), 155–174.

Etienne, D., Ruffaldi, P., Dupouey, J.L., Georges-Leroy, M., Ritz, F., Dambrine, E., 2013. Searching for ancient forests: a 2000 year history of land use in northeastern French forests deduced from the pollen compositions of closed depressions. Holocene 23 (5), 678–691.

Ferrier, K.L., Kirchner, J.W., 2008. Effects of physical erosion on chemical denudation rates: a numerical modeling study of soil-mantled hillslopes. Earth Planet. Sci. Lett. 272 (3), 591–599.

Fichter, J., Turpault, M.P., Dambrine, E., Ranger, J., 1998. Mineral evolution of acid forest soils in the Strengbach catchment (Vosges mountains, NE France). Geoderma 82 (4), 315–340.

Gangloff, S., Stille, P., Pierret, M-C., Weber, T., Chabaux, F., 2014. Characterization and evolution of dissolved organic matter in acidic forest soil and its impact on the mobility of major and trace elements (case of the Strengbach watershed). Geochim. Cosmochim. Acta 130, 21–41.

Gontier, A., Rihs, S., Chabaux, F., Lemarchand, D., Pelt, E., Turpault, M.-P., 2015. Lack of bedrock grain size influence on the soil production rate. Geochim. Cosmochim. Acta 166, 146–164.

Granet, M., Chabaux, F., Stille, P., Dosseto, A., France-Lanord, C., Blaes, E., 2010. U-series disequilibria in suspended river sediments and implication for sediment transfer time in alluvial plains: the case of the Himalayan rivers. Geochim. Cosmochim. Acta 74 (10), 2851–2865.

Gy, P.M., 1992. Sampling of Heterogeneous and Dynamic Material Systems: Theories of Heterogeneity, Sampling and Homogenizing. Elsevier.

Heimsath, A.M., Chappell, J., Dietrich, W.E., Nishiizumi, K., Finkel, R.C., 2000. Soil production on a retreating escarpment in southeastern Australia. Geology 28 (9), 787–790.

Heyman, B.M., Heyman, J., Fickert, T., Harbor, J.M., 2013. Paleo-climate of the central European uplands during the last glacial maximum based on glacier mass-balance modeling. Quat. Res. 79 (1), 49–54.

Jin, L., Ravella, R., Ketchum, B., Bierman, P.R., Heaney, P., White, T., Brantley, S.L., 2010. Mineral weathering and elemental transport during hillslope evolution at the Susquehanna/Shale Hills Critical Zone Observatory. Geochim. Cosmochim. Acta 74 (13), 3669–3691.

Kim, K.J., Englert, P.A.J., 2004. Profiles of in situ ^{10}Be and ^{26}Al at great depths at the Macraes Flat, East Otago, New Zealand. Earth Planet. Sci. Lett. 223 (1), 113–126.

Leroy, S.A.G., Zolitschka, B., Negendank, J.F., Seret, G.U.Y., 2000. Palynological analyses in the laminated sediment of Lake Holzmaar (Eifel, Germany): duration of Lateglacial and Preboreal biozones. Boreas 29 (1), 52–71.

Ma, L., Chabaux, F., Pelt, E., Blaes, E., Jin, L., Brantley, S., 2010. Regolith production rates calculated with uranium-series isotopes at Susquehanna/Shale Hills Critical Zone Observatory. Earth Planet. Sci. Lett. 297 (1), 211–225.

Marquardt, D.W., 1963. An algorithm for least-squares estimation of nonlinear parameters. J. Soc. Ind. Appl. Math. 11 (2), 431–441.

McDowell, W.H., Asbury, C.E., 1994. Export of carbon, nitrogen, and major ions from three tropical montane watersheds. Limnol. Oceanogr. 39 (1), 111–125.

Mercier, J.L., Bourlès, D.L., Kalvoda, J., Braucher, R., Paschen, A., 1999. Deglaciation of the Vosges dated using ^{10}Be. Acta Univ. Carol., Geogr. 2, 139–155.

Nishiizumi, K., Winterer, E.L., Kohl, C.P., Klein, J., Middleton, R., Lal, D., Arnold, J.R., 1989. Cosmic ray production rates of ^{10}Be and ^{26}Al in quartz from glacially polished rocks. J. Geophys. Res., Solid Earth (1978–2012) 94 (B12), 17907–17915.

Pelt, E., Chabaux, F., Stille, P., Innocent, C., Ghaleb, B., Gérard, M., Guntzer, F., 2013. Atmospheric dust contribution to the budget of U-series nuclides in soils from the Mount Cameroon volcano. Chem. Geol. 341, 147–157.

Prunier, J., Chabaux, F., Stille, P., Pierret, M.C., Viville, D., Gangloff, S., 2015. Monitoring of geochemical and isotopic (Sr, U) signatures in soil solutions for the evaluation of soil weathering evolution (the Strengbach case). Chem. Geol. 417, 289–305.

Riebe, C.S., Kirchner, J.W., Finkel, R.C., 2003. Long-term rates of chemical weathering and physical erosion from cosmogenic nuclides and geochemical mass balance. Geochim. Cosmochim. Acta 67 (22), 4411–4427.

Rihs, S., Prunier, J., Thien, B., Lemarchand, D., Pierret, M.C., Chabaux, F., 2011. Using short-lived nuclides of the U- and Th-series to probe the kinetics of colloid migration in forested soils. Geochim. Cosmochim. Acta 75 (23), 7707–7724.

Schaller, M., Von Blanckenburg, F., Veldkamp, A., Tebbens, L.A., Hovius, N., Kubik, P.W., 2002. A 30 000 yr record of erosion rates from cosmogenic ^{10}Be in Middle European river terraces. Earth Planet. Sci. Lett. 204 (1), 307–320.

Schoonejans, J., Vanacker, V., Opfergelt, S., Granet, M., Chabaux, F., 2016. Coupling uranium series and ^{10}Be cosmogenic radionuclides to evaluate steady-state soil thickness in the Betic Cordillera. Chem. Geol. http://dx.doi.org/10.1016/j.chemgeo.2016.03.030. In press.

Seret, G., Dricot, E., Wansard, G., 1990. Evidence for an early glacial maximum in the French Vosges during the last glacial cycle. Nature 346 (6283), 453–456.

Siame, L., Bellier, O., Braucher, R., Sébrier, M., Cushing, M., Bourlès, D., Yiou, F., 2004. Local erosion rates versus active tectonics: cosmic ray exposure modelling in Provence (south-east France). Earth Planet. Sci. Lett. 220 (3), 345–364.

Small, E.E., Anderson, R.S., Hancock, G.S., 1999. Estimates of the rate of regolith production using ^{10}Be and ^{26}Al from an alpine hillslope. Geomorphology 27, 131–150.

Stille, P., Pourcelot, L., Granet, M., Pierret, M.-C., Perrone, Th., Morvan, G., Chabaux, F., 2011. Deposition and migration of atmospheric Pb in soils from a forested silicate catchment today and in the past (Strengbach case; Vosges mountains); evidence from ^{210}Pb activities and Pb isotope ratios. Chem. Geol. 289, 140–153. http://dx.doi.org/10.1016/j.chemgeo.2011.07.021.

Viville, D., Chabaux, F., Stille, P., Pierret, M.C., Gangloff, S., 2012. Erosion and weathering fluxes in granitic basins: the example of the Strengbach catchment (Vosges massif, eastern France). Catena 92, 122–129.

West, N., Kirby, E., Bierman, P., Slingerland, R., Ma, L., Rood, D., Brantley, S., 2013. Regolith production and transport at the Susquehanna Shale Hills Critical Zone Observatory, part 2: insights from meteoric ^{10}Be. J. Geophys. Res., Earth Surf. 118 (3), 1877–1896.

WRB (International Union of Soil Sciences Working Group WRB), 2006. World Reference Base for Soil Resources 2006. World Soil Resources Reports No. 103. FAO, Rome.